MATERIALS PHYSICS AND MECHANICS RESEARCH ARTICLE

Submitted: December 18, 2025 **Revised: March 9, 2026** **Accepted: April 29, 2026**

Thermal-mechanical response to plunge depth variation in friction stir lap welding of AA6061 and SS304-computational fluid dynamics approach

A. Yadav ✉, **A. Jain, R. Verma**

NIT Kurukshetra, Kurukshetra, India

✉ amit.insan77@gmail.com

ABSTRACT

The influence of plunge depth on key thermo-mechanical performance indicators during dissimilar friction stir lap welding of AA6061 and SS304 using a finite volume method-based computational fluid-dynamics model is investigated. Simulations were conducted for plunge depth values ranging from 0 to 0.45 mm while maintaining constant rotational speed (1200 rpm), traverse speed (100 mm/min), and tool tilt angle (1.5°). The results show that the maximum workpiece temperature remains nearly constant at ~ 978 K across all plunge depth values, indicating minimal influence of plunge depth on overall heat generation. However, weld interface characteristics vary significantly with plunge depth. The maximum weld interface temperature increases from 743 to 791 K (~ 6.5 %), demonstrating enhanced interfacial heat transfer. Similarly, the maximum weld interface velocity increased from 0.07865 to 0.08121 m/s (~ 3.25 %), indicating improved material flow. In contrast, the minimum weld interface viscosity decreases from 8.94×10^5 to 6.82×10^5 kg/(ms) (~ 23.7 %), reflecting increased material softening. Tool-workpiece interface torque reduces from 14.96 to 13.91 Nm (~ 7 %), suggesting lower resistance to tool motion. These findings indicate that increasing plunge depth enhances bonding and material mixing, with an optimal plunge depth range of 0.15–0.30 mm for balanced weld quality and stability.

KEYWORDS

friction stir weld • computational fluid-dynamics • finite-volume approach • ANSYS • fluent

Citation: Yadav A, Jain A, Verma R. Thermal-mechanical response to plunge depth variation in friction stir lap welding of AA6061 and SS304-computational fluid dynamics approach. *Materials Physics and Mechanics*. 2026;54(3): 148–162. http://dx.doi.org/10.18149/MPM.5432026_12

Introduction

The automotive, aerospace and marine industries need lightweight structures with improved wear resistance to ensure optimal performance and longevity [1]. These specific uses illustrate the possibility of creating hybrid structures by using light materials such as aluminum alloys (AAs) in combination with stainless steel (SS) [2]. In order to provide a practical solution [3], using SS and AA joints strategically in important places. Researchers employed a number of new joining ways to join materials that were difficult to join, or that were not the same [4–6]. The use of friction stir welding (FSW), which was developed and patented by the Welding Institute UK in 1991, is a promising solution, as it overcomes the conventional fusion welding techniques due to the following advantages: reduced heat input, reduced thickness of intermetallic compounds (IMCs), and enhanced surface characteristics [7–9].

As shown in Fig. 1, the spinning tool is slowly pushed into workpiece until shoulder is fully in contact with it. This position is held until the necessary temperature is reached,

© A. Yadav, A. Jain, R. Verma, 2026.
Publisher: Peter the Great St. Petersburg Polytechnic University
This is an open access article under the CC BY-NC 4.0 license (https://creativecommons.org/li-censes/by-nc/4.0/)

which happens through frictional heating and plastic deformation. To make the necessary weld, the tool is moved along the weld line. The side of the rotating tool where the tangential velocity coincides with the traverse speed (TRS) is referred to as the advancing side (AS). The retreating side (RS) refers to the side of a rotating tool that has a vectorial sense opposite to the tangential velocity and TRS. The workpiece section located ahead of the tool is known as the leading side, and the section located behind the tool is known as the trailing side. FSW generates welds without the melting of the base material, hence eliminating the risks of solidification cracking, deformation, porosity, and other related issues. It necessitates no edge preparation and generates transition junctions between dissimilar metals [10].

The primary restriction of FSW is its necessity for distinct tools corresponding to varying workpiece thicknesses, and the resultant exit hole that remains upon the withdrawal of the tool from the workpiece. Large forces on the clamp, necessitate robust gripping. It is mainly limited to linear welding. Additionally, filler joints cannot be achieved with FSW [10].

Most existing studies focus on parameters such as rotational speed, traverse speed, and tool tilt angle, emphasising microstructure and mechanical properties [11–14]. In contrast, plunge depth (PD), which directly affects tool penetration, interfacial contact, and heat transfer, has not been systematically studied in relation to fundamental thermo-mechanical responses [15]. A clear research gap exists in linking PD with key interface-level parameters such as temperature, material flow velocity, viscosity, and torque, particularly for AA6061–SS304 lap joints. To address this, the present study uses an FVM-based computational fluid-dynamics (CFD) model to examine the influence of PD on maximum weld interface temperature (MWIT), maximum weld interface velocity (MWIV), minimum weld interface viscosity (MWIVis), and tool-workpiece interface torque (TWIT) during dissimilar friction stir lap welding (DFSLW) of AA6061 and SS304.

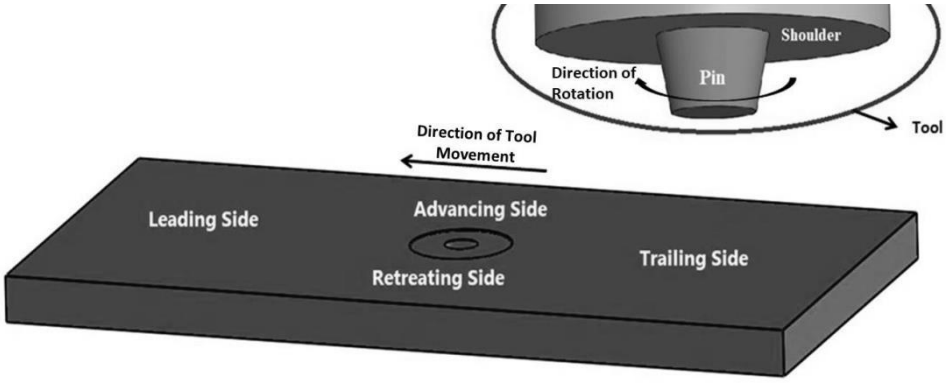


Fig. 1. Friction stir weld process

There has been a lot of research on dissimilar friction stir welding (DFSW) of AAs with SS, especially SS304 steel, in the last few years. This research has been directed towards the investigation of the interfacial microstructure, IMC formation and joint performance. Nishida et al. [16] studied the production of ultrafine IMC layers for the case of duplex stainless steel (DSS) between AA3003-H112 and SS304 with a thin but resilient reaction layer, and in which the reaction layer showed higher strength than the base

aluminium. Habibnia et al. [17] examined AA5050-SS304 butt welds and found that a reduction in tool rotational speed (ROS) and an increase in the feed rate improved the joint quality. In the same way, in a study of AA6061-SS304 butt welds, Ghosh et al. [18] observed that the iron content at the interface increased with higher heat input, altering the composition of the IMC from Fe_2Al_5 to Fe-rich phases such as Fe_3Al and $FeAl_2$, which was the point of maximum strength at intermediate ROS.

Balamagendiravarman et al. [19,20] focused on the investigation of both AA-SS304 butt welds and commercially pure aluminium-SS304 welds with asymmetric microstructural changes, where the more significant changes in microstructure were observed on the aluminium side due to thermal-mechanical property discrepancies. It was shown that interfacial IMCs, including Al_3Fe, $FeAl_2$, Fe_4Al_{13}, Fe_2Al_5 and $FeAl_3$ formed, and the hardness was highest in the stir zone (SZ) because of IMCs formation. Under the best conditions the maximum tensile strength was 90 % of the base aluminum.

Researchers explored alterations of the FSW process, such as underwater friction stir welding (UFSW). Mahto et al. [21,22] showed that faster cooling in UFSW stopped the growth of IMC and made the material less porous and improved the microstructure, resulting in less porous material. Their later work on lap welds of AA6061-SS304 showed that as ROS and PD went up, the grains got finer. However, they also found that the welds were more likely to corrode due to the finer grain boundaries as well as small pits. Chitturi et al. [23] stressed how important the tool tilt angle (TA) and pin depth are for getting rid of weld defects and encouraging IMC formation. The hardness values in the SZ were 3 times higher than in SS304.

Researchers investigated fatigue and fracturing performance. Uematsu et al. [24] found that fatigue crack propagation behaviour was not as effective in AA6061-SS304 butt welds compared to the aluminium base metal but had consistent trends using effective stress intensity factors. Chitturi et al. [25] showed that TA has a significant effect on the behaviour of fracture, which the IMCs, such as AlFe and $AlFe_3$ can be confirmed by X-ray diffraction (XRD), has a crucial role in the hardness value as high as 630 HV values. Jabraeili et al. [26] found that the tool offset had a big effect on the quality of the weld. Positive offsets resulted in the formation of tunnel defects, whereas negative offsets resulted in the formation of thick IMCs. The best offsets made serrated interfaces and thin IMCs, which made joints that were more flexible.

These results are borne out in other studies. Wang et al. [27] showed that tool offset had a bigger effect on the properties of the joint than ROS in AA3003-SS304 welds. Joshani et al. [28] showed a rise in IMC thickness, which was related to higher ROS in AA7075-SS304 welds, resulting in a decrease in strength. Datta et al. [29] compared AA1100-SS304 and AA7075-SS304 welds and found that AA1100 had better joint efficiency and elongation. Kumar et al. [30] found that ROS and TRS are the most important factors that affect IMC thickness, tensile strength, and microstructural refinement.

Thermal and numerical analyses have provided further information in addition to experimental work. Ou et al. [31] investigated heat transfer in dissimilar AA6061-SS304 FSW using a CFD model that uniquely incorporated the weld tool. Validated through IR thermography and SEM, the model reduced peak temperature prediction error to 2.3 % (compared to 11.4 % without the tool), minimised temperature gradients and inhomogeneity across the interface, and more accurately captured the effect of TRS on

IMC formation. The study demonstrated that including the weld tool improved predictions of stirring efficiency, viscosity variations, and overall weld quality. Mir et al. [2,9,32] showed that tool ROS is very important in controlling wear resistance, microhardness, and corrosion behavior with grain refinement leading to improved performance. Zhang et al. [33] reported on the inhibition of detrimental Cu rich IMCs in AA2219-SS304 welds at low rates of oxidation, which produced defect-free joints with improved tensile strength. Research made by Nakrani et al. [34] and Caetano et al. [35] called the fatigue crack propagation and the joint geometry, showing how susceptible DFSW performance is to tool alignment and axial force.

A review of the current literature shows that most of the studies have focused on microstructure evolution, IMC formation and mechanical response of dissimilar aluminium and steel joints. In order to do this, researchers have carefully examined the impact of various process parameters, such as tool ROS, TRS, TA and offset, on the strength and integrity of the joint. However, there are some notable gaps in research. First, although PD has been associated with heat generation and microstructural changes, its effect on fundamental thermo-mechanical performance measures (such as MWIT, MWIV, MWIVis, and TWIT) has not been well explored. Second, weld interface viscosity (controls material mixing, flow stability, and formation of defects) has not previously been thoroughly investigated for AA6061 ss 304 lap joints. Third, torque, a direct measure of tool-workpiece interaction and energy consumption, has not been systematically correlated with PD or weld quality in this material system. Finally, most existing research has emphasised butt joints or alternative aluminium alloys (AA2024, AA5052, AA7075), leaving limited insight into the industrially relevant lap weld configuration of AA6061-SS304.

Addressing these gaps necessitates a physics-based investigation into the role of PD on key thermo-mechanical performance parameters in DFSLW of AA6061 with SS304. The current study employs finite volume method (FVM) simulations in ANSYS Fluent to evaluate MWIT, MWIV, MWIVis, and TWIT, offering new insights into heat generation, material flow, and tool-workpiece interaction. The novelty of this study lies in its CFD-based, physics-driven analysis of PD in DFSLW of AA6061-SS304. Unlike previous studies that mainly focus on experimental observations of microstructure, intermetallic formation, and mechanical properties, this work directly evaluates the effect of PD on key thermo-mechanical parameters such as MWIT, MWIV, MWIVis, and TWIT. The results have practical relevance for automotive and aerospace applications, where aluminium-steel lap joints are widely used.

Simulation design

The simulation model utilises an AA6061 sheet and an SS304 sheet with dimensions of 200 × 75 × 3 mm^3 (each sheet). They are joined in a lap arrangement with an overlap width of 30 mm (Fig. 2). Solidworks® 2017 is used for geometric modelling, while CFD software ANSYS® 19.3 R3 (FLUENT®) is employed for FVM numerical simulation [36]. A flat shoulder tool with a frustum conical pin is employed (Table 1). The material used for the tool is tungsten carbide.

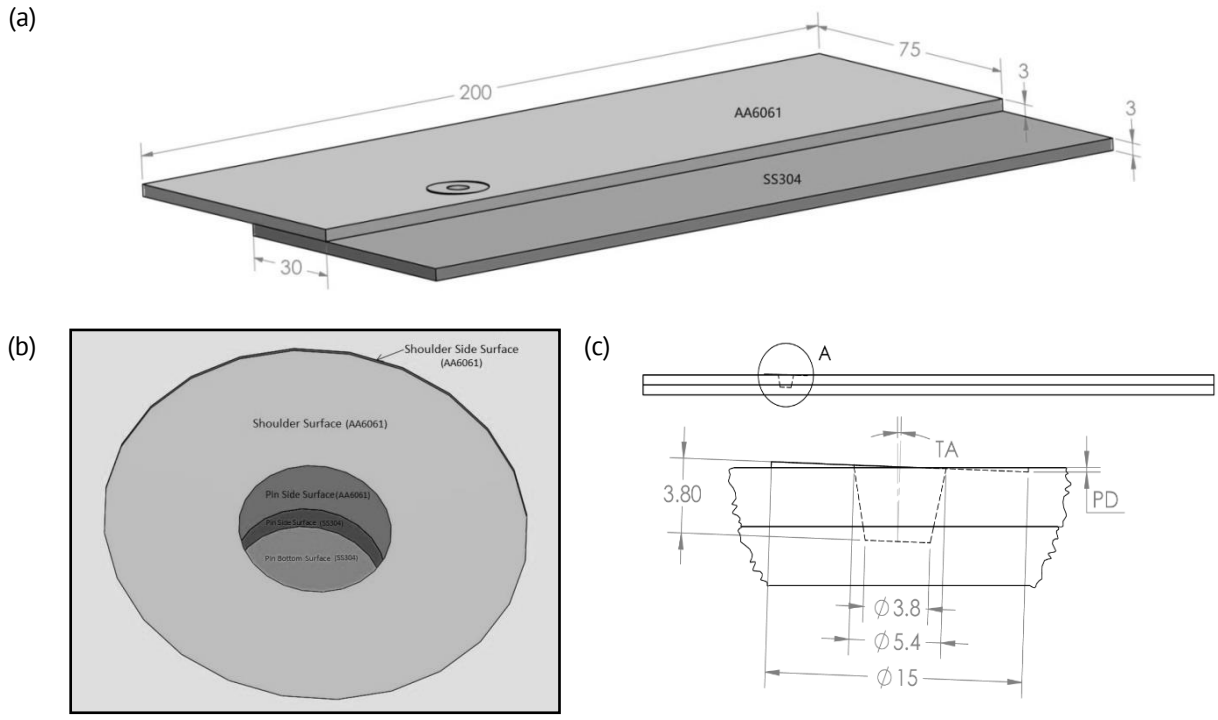


Fig. 2. (a) Arrangement of dissimilar friction stir lap weld of AA6061 with SS304; (b) tool-workpiece interface surfaces; (c) dimensions of the tool employed

Table 1. Fixed process parameters

Process parameter	Value
Diameter of flat shoulder, mm	15.0
Pin length, mm	3.8
Pin base diameter, mm	5.4
Pin tip diameter, mm	3.8
TA, °	1.5
Overlap width, mm	30.0

The realisable k-epsilon viscous model is employed to simulate the flow of material in a transient state [37]. The realisable k-ε model is chosen because it provides better stability and accuracy for rotational and shear-driven flows compared to the standard k-ε model. It improves the prediction of strain rates and flow separation, which are critical for representing material stirring and interfacial mixing in FSW. This makes it suitable for approximating the complex flow patterns around the rotating tool, especially in CFD frameworks like ANSYS Fluent®. A mesh with tetrahedron cells is utilised, with a fine mesh at the interface between the tool and the workpiece, as depicted in Fig. 3 [38]. The grid independence test is performed using meshes with 99260, 107676, 118766, 134823, 157280, 187342, and 208214 nodes. Among these, a mesh comprising 187342 nodes is found to be sufficient to accurately capture the essential temperature and material flow characteristics and is therefore adopted for all subsequent simulations. The mesh refinement study conducted is illustrated in Fig. 3(c). The present work adheres to the following assumptions:

I. The process is a quasi-steady process, i.e., the rate of heat generation remains constant.

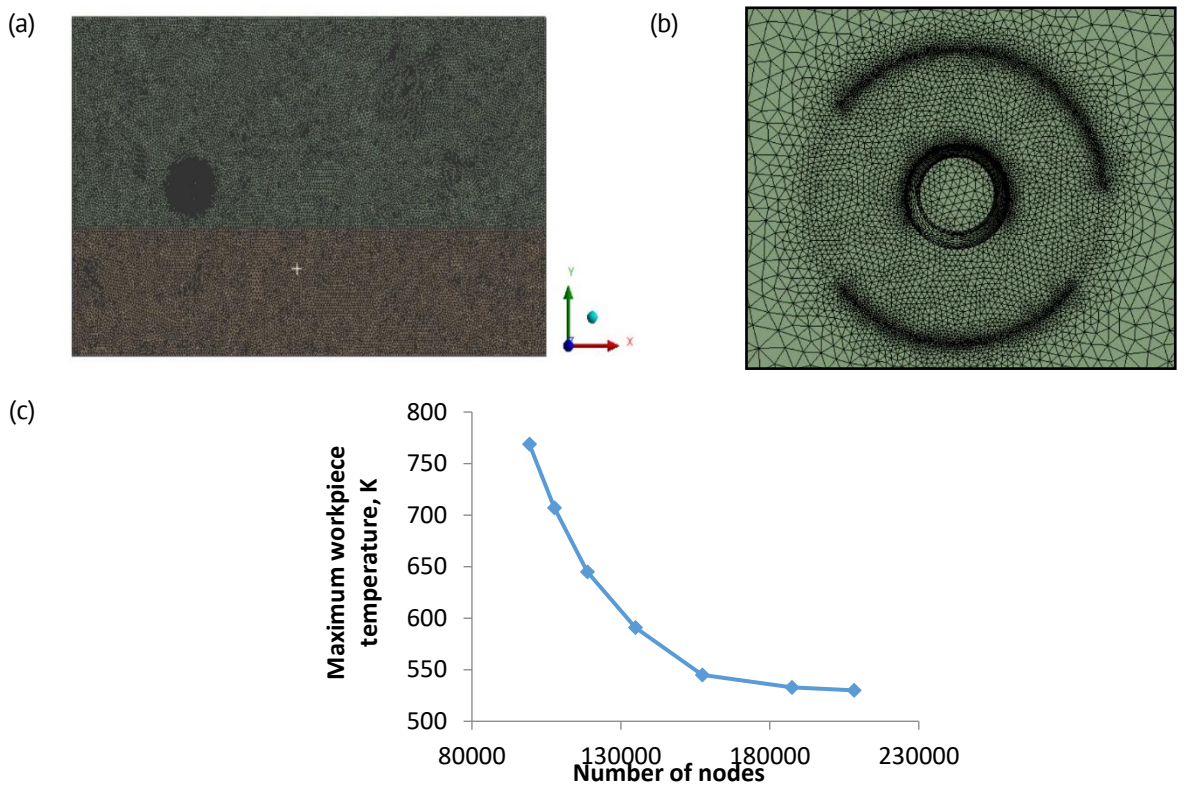


Fig. 3. (a) Tetrahedron cells' mesh used in the model; (b) close-up view (top) of tool-workpiece interface; (c) grid independence test at ROS of 200 rpm, TRS of 100 mm/min, TA of 1.5° and PD of 0.225 mm

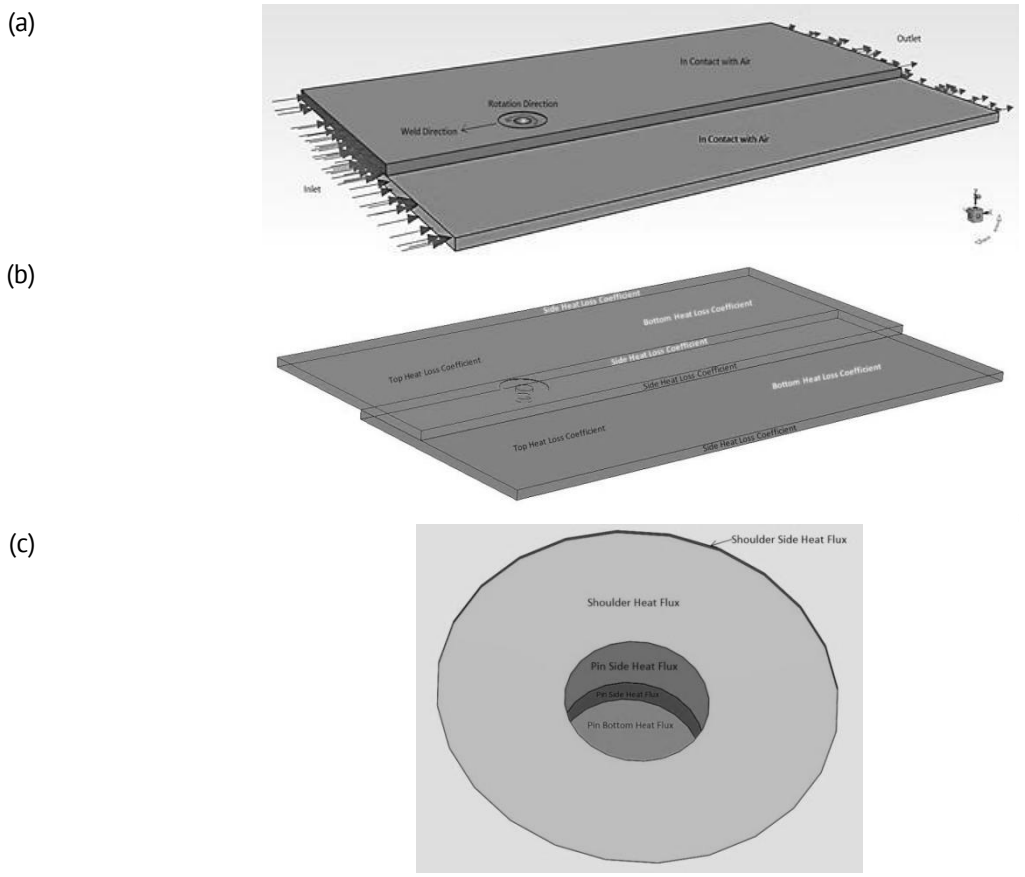


Fig. 4. (a) Flow directions of materials in the model; (b) different heat loss surfaces of the model; (c) different heat flux generating surfaces of the model

II. Material that has undergone plasticization is classified as non-Newtonian, incompressible, and visco-plastic.
III. The material is presumed to exhibit characteristics of a non-Newtonian fluid, where its viscosity is influenced by both temperature and strain rate.
IV. Partial slip condition exists between the tool and the workpiece.
V. Free slip condition exists on the upper, bottom, and side surfaces of the workpiece.
VI. The outlet boundary assumes a value of zero pressure.

To make precise predictions about welding, it is crucial to employ realistic boundary conditions [39,40]. Figure 4 displays the parts and boundaries imposed on the model.

The inlet boundary condition of flow is taken from [40]. Tool periphery velocity when tool TA (ξ) and contact state variable (δ) are considered, are represented by equations below [41]. Equations (1)–(3) are used to define the momentum boundary conditions at the tool-workpiece interface, specifically at the shoulder surface (SS), pin side surface (P_{SS}), and pin bottom surface (P_{BS}):

$$u_i = (1-\delta)((\omega r sin\theta)\cos\xi - u_{weld}, \quad (1)$$

$$v_i = (1-\delta)\omega r cos\theta, \quad (2)$$

$$w_i = (1-\delta)(\omega r \sin\theta)\sin\xi, \quad (3)$$

$\delta_{AA6061} = \left(0.31e^{\omega r/1.87} - 0.026\right)$ (from [42]) and $\delta_{SS304} = 0.7$ (from [43]). (4)

The viscosity (η) is determined using the equations below [44–46]:

$$\eta = \frac{\sigma}{3\bar{\varepsilon}}, \quad (5)$$

$$\sigma\ (\text{flow stress}) = \frac{1}{\beta}\ln\left\{\left(\frac{Z}{A}\right)^{\frac{1}{n}} + \left(1 + \left(\frac{Z}{A}\right)^{\frac{2}{n}}\right)^{\frac{1}{2}}\right\}, \quad (6)$$

$$Z\ (\text{Zener Hollomon parameter}) = \bar{\varepsilon}e^{\left(\frac{Q}{RT}\right)}, \quad (7)$$

$$\bar{\varepsilon}\ (\text{strain rate}) = \left(\frac{2}{3}\varepsilon_{ij}\varepsilon_{ij}\right)^{\frac{1}{2}}, \quad (8)$$

where T represents temperature, measured in Kelvin (K); A, β, and n are constants that describe the material properties; Q is an activation energy that does not depend on temperature; R is the gas constant.

Table 2 provides the material constants and properties of AA6061 [47]. Equation (7) is used to define the viscosity as a function of temperature and strain rate for the given materials, namely AA6061 and SS304. These equations are implemented through the use of User Defined Functions.

Table 2. Material-constants and properties for AA6061 and SS304 [41,43,48–50]

Parameters		**AA6061**	**SS304**
Material constants	A, s^{-1}	2.41×10^8	1.62×10^{16}
	n	3.55	6.1
	Q, $J \cdot mol^{-1}$	1.45×10^5	4.46×10^5
	β, MPa^{-1}	0.0367	0.008
Material density ρ, $kg \cdot m^{-3}$		2700	7400
Top (h_t) and side (h_s) heat transfer coefficient, W/m^2K		80	0.0668T
Bottom (h_b) heat transfer coefficient, W/m^2K		150	10×0.0668T
External emissivity of workpiece top surface		0.09	0.17

The heat created during the FSW process is distributed over many regions. The tool's contacting surface with the workpiece is partitioned into three sections: bottom *SS*, P_{SS}, and P_{BS} (Fig. 4(c)). The SS is subdivided into two sections: shoulder with conical surface (S_{CS}) and shoulder with flat surface (S_{FS}). All these sections exhibit partial sticking-sliding contact. Heat produced from different sources is provided below:

$$Q_{total} = \delta Q_{sticking} - (1-\delta) Q_{sliding}. \quad (9)$$

When the slip coefficient (δ) is equal to zero, heat is only generated through friction. When the value of δ is equal to 1 (indicating a stick), all heat is produced only through the deformation of the plastic material [51].

The assumed maximum yielding shear stress is [52]:

$$\tau_b = \frac{\sigma_s}{\sqrt{3}}, \quad (10)$$

$$(\sigma_s)_{AA6061} = 1160 - 8.88T + 2.97 \times 10^{-2} T^2 - 3.32 \times 10^{-5} T^3 \text{ (from [49])}, \quad (11)$$

$$(\sigma_s)_{SS304} = 796 - 1.6T + 2.25 \times 10^{-3} T^2 - 1.3 \times 10^{-6} T^3 \text{ (from [43])}, \quad (12)$$

where σ_s represents the material's yield stress.

The heat-flux (W/m^2) in S_{CS} section is ([41,43,48,49]):

$$q_{S_{CS}} = \eta \left(\frac{[(1-\delta_{CSS})\tau_b + (\delta_{CSS})\mu P] 2\omega [(r_1^3 - r_2^3)(1+\tan\propto')]}{3(r_1^2 - r_2^2)} \right). \quad (13)$$

Heat-flux (W/m^2) in P_{SS} section is:

$$q_{P_{SS}} = \eta((\omega r - v sin\theta)((1-\delta_{PSS})\tau_b + (\delta_{PSS})\mu P)). \quad (14)$$

Heat-flux (W/m^2) in P_{BS} section is:

$$q_{P_{BS}} = \eta \left(\frac{2\omega r_3((1-\delta_{PBS})\tau_b + (\delta_{PBS})\mu P)}{3} \right), \quad (15)$$

where μ (0.4 is same for AA6061 and 0.5 for SS304) is the coefficient of friction [43,53]; *P* is plunge pressure (Pa); ω is ROS (rad/s); η is fraction of heat transferred to the workpiece (i.e., 0.6 and 0.4 for AA6061 and SS304, respectively [31]); and $\propto'$ is cone angle of shoulder ($\propto'$ = 0 for S_{FS})). A plunging pressure of 12 and 109 MPa is taken for AA6061 and SS304, respectively [43,53]. Equations (13)–(15) are used to define the thermal boundary conditions for the SS, P_{SS}, and P_{BS}, respectively.

The specific-heat (C_p) equation for AA6061 is shown below [42,43]:

$$(C_p)_{AA6061} = 929 - 0.627T + 1.481 \times 10^{-3} T^2 - 4.33 \times 10^{-8} T^3, \quad (16)$$

$$(C_p)_{SS304} = 276 + 0.851T - 8.51 \times 10^{-4} T^2 + 3.0 \times 10^{-7} T^3. \quad (17)$$

The thermal conductivity (k) equation for AA6061 is shown below [42,43]. Equations (16), (17) and (18), (19) are used to define C_p and k, respectively, as material properties for both AA6061 and SS304:

$$k_{AA6061} = 25.22 + 0.3978T + 7.358 \times 10^{-6} T^2 - 2.518 \times 10^{-7} T^3, \quad (18)$$

$$k_{SS304} = 14.3 - 9.02 \times 10^{-3} T + 4.52 \times 10^{-5} T^2 - 2.49 \times 10^{-8} T^3. \quad (19)$$

The boundary condition for heat exchange between the top surface of the workpiece and the environment is convective as well as radiative heat transfer [41]. The heat exchange between the bottom and side surfaces of the workpiece is conductive (due to contacts of jigs and fixtures) and convective heat transfer, respectively. All these heat exchanges are converted to convective form as shown below [41]:

$$k \frac{\partial T}{\partial z} = h_t (T - T_0), \quad (20)$$

$$k \frac{\partial T}{\partial z} = h_b (T - T_0), \quad (21)$$

$$k \frac{\partial T}{\partial z} = h_s (T - T_0), \quad (22)$$

where h_t, h_b and h_s are coefficients of heat dissipation at the workpiece's top, bottom and side surface, respectively; T_0 is the environmental temperature (300 K) [42]. Equations (18)–(20) are used to define the thermal boundary conditions for the top surface, bottom surface, and side surface of the workpiece, respectively [54–57].

Results and Discussion

Validation of the current model is done with the work by Wenmin Ou et al. [31]. A 3D CFD model was constructed to study the heat transfer in DFSBW of AA6061 with SS304 with a frustum conical pin tool. In the present study, the above work is replicated, and upon validation of the current methodology and procedure, additional fixed input parameters (TA and PD) are introduced. The temperature distribution data of the model closely corresponds to the experimental data of Wenmin Ou et al. [31]. Table 3 compares the temperature of the experimental and model. Thus, the numerical modelling method is satisfactory.

Table 3. Comparison results between experimental [31] and modelled temperature

Points (approx.)	Experimental temperature, K	Simulation model temperature, K	Error, %
p1(8.99,0.5,3)	492.3	469.6	4.61
p2(8.94,1,3)	475.1	455.3	4.16
p3(-8.06,4,3)	439.4	429.4	2.27

The velocity and viscosity values presented in Table 4 correspond to the interfacial region of both materials, namely AA6061 aluminium and SS304 steel. This region represents the zone where intermixing occurs during the friction stir lap welding process, leading to the formation of intermetallic compounds. Simulation experiments were conducted for various values of ROS as process parameters to compute MWIT, MWIV, MWIVis, and TWIT performance measures for each. Columns 4, 5, 6, and 7 of Table 4 indicate the MWIT, MWIV, MWIVis, and TWIT obtained in each experiment, respectively. The analysis of results is discussed below.

Table 4. Experimental design and its results

S. No.	PD, mm	Maximum workpiece temperature, K	MWIT, K	MWIV, m/s	MWIVis, Kg/(ms)	TWIT, Nm
1	0	978	743	0.07865	8.94E+05	14.96
2	0.15	978	756	0.07951	7.94E+05	14.74
3	0.3	978	773	0.08037	7.26E+05	14.60
4	0.45	978	791	0.08121	6.82E+05	13.91

Effect of PD on MWIT

Figure 5 graph shows the variation of temperature with PD. The two parameters plotted are MWIT and maximum workpiece temperature. Maximum Workpiece Temperature (red line) remains constant at around 978 K across all PDs (0 to 0.45 mm). This means that PD has very little effect on the highest temperature reached in the workpiece. The maximum temperature stays the same, which means that the thermal energy input from ROS and TRS is the most important factor, and PD doesn't change the overall heat generation very much.

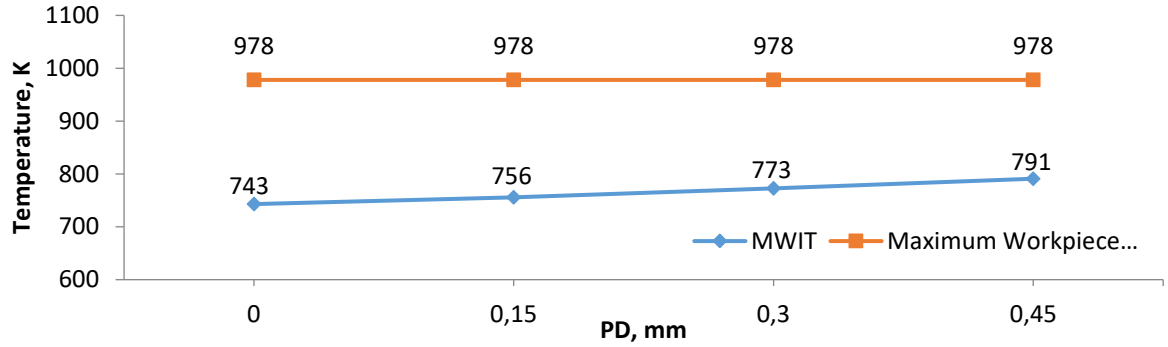


Fig. 5. Effect of PD process parameter on MWIT performance measure

The blue line for MWIT shows a slow rise from 743 K at 0 mm PD to 791 K at 0.45 mm PD. This means that as PD goes up, the area where the workpieces meet gets a little bit hotter. This is because the tool and workpiece are in better contact, which makes heat transfer better at the interface and makes the material more plastic.

Implications for weld quality. The increase in MWIT with PD indicates better bonding conditions at the interface which reduces the possibility of incomplete fusion or formation of voids. Increasing PD doesn't risk overheating the workpiece too much, as the maximum temperature remains the same. Overheating could harm the properties of the material. So, PD mostly increases the quality of the bond between both the surface without making the weld area less stable in terms of temperature.

Effect of PD on MWIV

The effect of PD on MWIV is shown in the graph of Fig. 6. The plot shows that MWIV is increasing steadily as PD is increasing, going from 0.07865 m/s at 0 mm PD to 0.08121 m/s at 0.45 mm PD. The positive slope indicates an improvement in the flow of material at the weld interface with deeper PDs, as the tool penetrates better and transfers more shear forces to the workpiece. This increased speed at the interface means that stirring is better, which helps materials mix and deform better.

Implications for weld quality. Higher MWIV at higher PDs ensure that the material flows better and sticks together better at the joint interface, reducing the occurrence of defects such as voids or weak bonding. The trend demonstrates that PD is an important

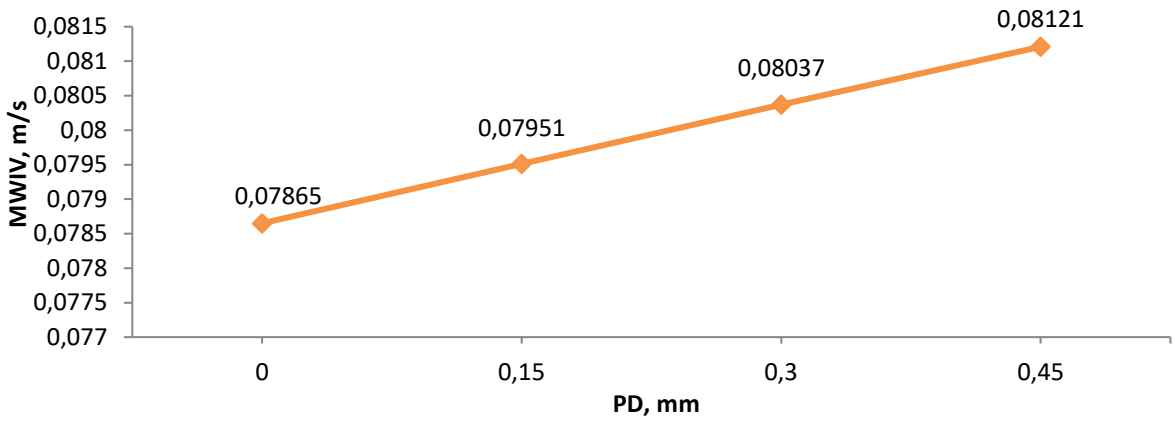


Fig. 6. Effect of PD process parameter on MWIV performance measure

factor in controlling the speed of the interface, which directly has an impact on the strength and quality of the weld. But more PD does make MWIV better, too much penetration can wear out tools or cause distortion in thin areas, so it needs to be optimised to make sure there are no defects in the welds.

Effect of PD on MWIVis

Figure 7 shows the variation of MWIVis with PD. From the plot, it is evident that MWIVis decreases consistently as PD increases. The values drop from 8.94 × 10^5 Kg/ms at 0 mm PD to 6.82 × 10^5 Kg/ms at 0.45 mm PD. This trend suggests that as the tool plunges deeper, the localised temperature at the interface increases, which in turn lowers the viscosity of the workpiece material. Lower viscosity indicates that the material at the weld interface becomes more plastic and easier to deform, enhancing material flow.

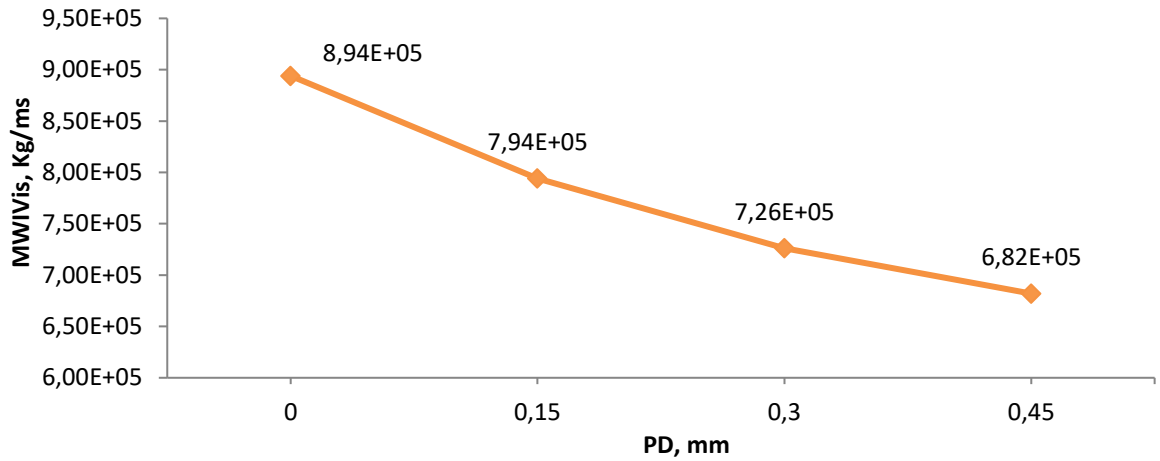


Fig. 7. Effect of PD process parameter on MWIVis performance measure

Implications for weld quality. The reduction in MWIVis with increasing PD favours better stirring and mixing of the base materials, thereby improving metallurgical bonding. Enhanced plastic flow reduces the likelihood of interfacial defects, such as voids or weak adhesion, which are often caused by insufficient material softening. However, if viscosity decreases excessively, it may lead to over-softening or excessive flash formation, which could compromise weld surface finish and dimensional accuracy.

Effect of PD on TWIT

Figure 8 shows the change in TWIT as a function of PD. Based on the observed trend, TWIT declines with the increasing PD. Torque decreases with 14.96 Nm at 0 mm PD to 13.91 Nm at 0.45 mm PD. Slow torque decreases means that increased PD decreases the resistance that the workpiece presents to the tool rotation process. This is attributed to high rate of softening the material, which is caused by high interface temperature and low viscosity as in the above graphs. The decrease is quite small until 0.3 mm PD, when it increases more strongly to 0.45 mm PD, and is nonlinear in the effect of PD.

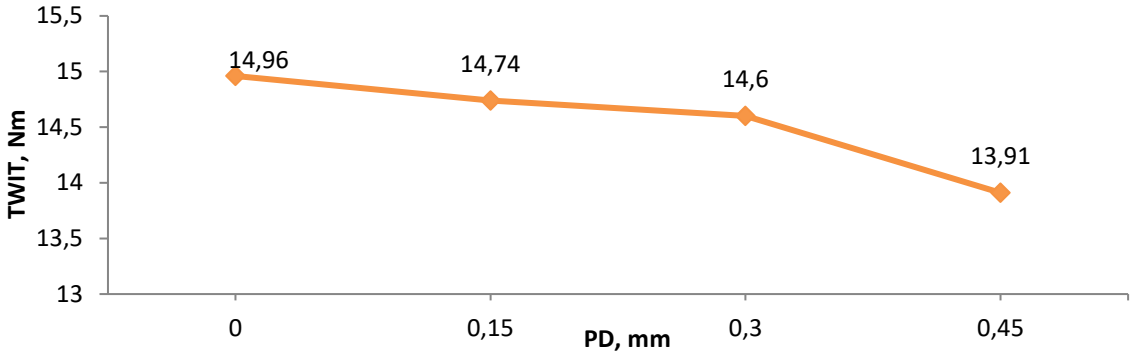


Fig. 8. Effect of PD process parameter on TWIT performance measure

Implications for weld quality. Lower torque at higher PDs means that tool penetration is easier and material plasticization is better, which is favourable for smooth stirring action. The decrease of the torque is consistent with the decrease in the viscosity, which suggests the better flowing characteristic of the material. However, excessively low torque can be a signal of over-softening, which can contribute to the formation of flashes or a lack of weld dimensional stability. Therefore, there is an optimum PD range in which torque is low enough for an effective stirring action but not so low as to affect the quality of the weld.

Conclusions

The present study systematically evaluated the influence of PD on key thermo-mechanical performance indicators (MWIT, MWIV, MWIVis, and TWIT) during DFSLW of AA6061 and SS304. The results demonstrate that while the maximum workpiece temperature remains nearly constant at ~ 978 K across the investigated PD range (0–0.45 mm), the weld interface characteristics are significantly affected by PD.

Quantitatively, MWIT increased from 743 K at 0 mm PD to 791 K at 0.45 mm PD (~ 6.5 % rise), indicating improved interfacial heat transfer and plasticisation. Similarly, MWIV showed a steady increase from 0.07865 to 0.08121 m/s (~ 3.25 %), reflecting enhanced material flow and stirring efficiency. In contrast, MWIVis decreased from 8.94×10^5 to 6.82×10^5 kg/(m·s) (~ 23.7 % reduction), confirming progressive softening of the material at higher PD. TWIT also declined from 14.96 to 13.91 Nm (~ 7 % reduction), indicating reduced resistance due to improved plastic deformation.

These trends collectively indicate that increasing PD improves interfacial bonding conditions, promotes better material mixing, and reduces flow resistance. However, beyond a certain limit, excessive reduction in viscosity and torque may lead to over-softening, flash formation, and potential dimensional instability. Based on the combined thermo-mechanical response, an optimal plunge depth range of 0.15 to 0.30 mm is identified for practical applications.

CRediT authorship contribution statement

Amit Yadav: writing – original draft, conceptualization, investigation, data curation; **Ajai Jain**: writing – review & editing, supervision, data curation; **Rajiv Verma**: writing – review & editing, conceptualization, supervision, data curation.

Conflict of interest

The authors declare that they have no conflict of interest.

References

1. Tisza M, Czinege I. Comparative study of the application of steels and aluminium in lightweight production of automotive parts. *International Journal of Lightweight Materials and Manufacture*. 2018;1(4): 229–238.
2. Mir FA, Khan NZ, Nisar L, Khan HA, Alrokayan SH. Analyzing microstructural evolution and wear behavior of friction stir welded dissimilar joints of SS304 and 2024-T3 Al alloy. *Materials Letters*. 2024;366: 136493.
3. Kusuda Y. Honda develops robotized FSW technology to weld steel and aluminum and applied it to a mass-production vehicle. *Industrial Robot: An International Journal*. 2013;40(3): 208–212.
4. Bajić D, Čekerevac D, Marjanović M, Perković S, Fidanovski B, Rigueiro C. Selected technical ceramics as nanoreinforcement for polyvinyl butyral/epoxy polymer composites. *Tribology and Materials*. 2023;2(2): 46–54.
5. Damlacik S, Baydi Z, Küpeli S, Kaplan D, Akan RŞ, Uludağ M. Study on mechanical and microstructural properties of advanced high-strength welded sheet metal. *Tribology and Materials*. 2023;2(2): 68–77.
6. Klobčar D, Pušavec F, Bračun D, Garašić I, Kožuh Z, Vencl A, Trdan U. Influence of Friction Riveting Parameters on the Dissimilar Joint Formation and Strength. *Materials*. 2022;15(19): 6812.
7. Tsang S. Friction welding. In: Olson DL, Siewert TA, Liu S, Edwards GR. (Eds) *ASM Handbook. Volume 6: Welding, Brazing and Soldering*. Materials Park (OH): ASM International; 1993. p.315–317.
8. Heidarzadeh A, Mironov S, Kaibyshev R, Çam G, Simar A, Gerlich A, Khodabakhshi F, Mostafaei A, Field DP, Robson JD, Deschamps A, Withers PJ. Friction stir welding/processing of metals and alloys: A comprehensive review on microstructural evolution. *Progress in Materials Science*. 2021;117: 100752.
9. Mir FA, Khan NZ, Parvez S, Siddiquee AN. Investigations on surface properties of friction stir welded dissimilar AA2024-T3 and 304 stainless steel joints. *Tribology International*. 2024;193: 109312.
10. Nandan R, DebRoy T, Bhadeshia HKDH. Recent advances in friction-stir welding: Process, weldment structure and properties. *Progress in Materials Science*. 2008;53(6): 980–1023.
11. Sun Z, Wu CS, Kumar S. Determination of heat generation by correlating the interfacial friction stress with temperature in friction stir welding. *Journal of Manufacturing Processes*. 2018;31: 801–811.
12. Zhai M, Wu CS, Su H. Influence of tool tilt angle on heat transfer and material flow in friction stir welding. *Journal of Manufacturing Processes*. 2020;59: 98–112.
13. Jain R, Pal SK, Singh SB. A study on the variation of forces and temperature in a friction stir welding process: A finite element approach. *Journal of Manufacturing Processes*. 2016;23: 278–286.
14. Shi L, Wu CS. Transient model of heat transfer and material flow at different stages of friction stir welding process. *Journal of Manufacturing Processes*. 2017;25: 323–339.
15. Kamalvand E, Jabbari A, Reza SM, Mazdak S, Beygi R, Mohammadi S. Effect of friction stir welding parameters on the deep drawing of tailor-welded blanks (TWBs). *CIRP Journal of Manufacturing Science and Technology*. 2021;33: 91–99.
16. Nishida T, Ogura T, Nishida H, Fujimoto M, Takahashi M, Hirose A. Formation of interfacial microstructure in a friction stir welded lap joint between aluminium alloy and stainless steel. *Science and Technology of Welding and Joining*. 2014;19(7): 609–616.
17. Habibnia M, Shakeri M, Nourouzi S, Givi MKB. Microstructural and mechanical properties of friction stir welded 5050 Al alloy and 304 stainless steel plates. *The International Journal of Advanced Manufacturing Technology*. 2015;76: 819–829.
18. Ghosh M, Gupta RK, Husain MM. Friction stir welding of stainless steel to Al alloy: Effect of thermal condition on weld nugget microstructure. *Metallurgical and Materials Transactions A*. 2014;45: 854–863.
19. Balamagendiravarman M, Kundu S, Chatterjee S. An analysis of microstructure and mechanical properties on friction stir welded joint of dissimilar 304 stainless steel and commercially pure aluminium. *Archives of Metallurgy and Materials*. 2017;62(3): 1813–1817.
20. Murugan B, Thirunavukarasu G, Kundu S, Kailas SV, Chatterjee S. Interfacial Microstructure and Mechanical Properties of Friction Stir Welded Joints of Commercially Pure Aluminum and 304 Stainless Steel. *Journal of Materials Engineering and Performance*. 2018;27: 2921–2931.

21. Mahto RP, Gupta C, Kinjawadekar M, Meena A, Pal SK. Weldability of AA6061-T6 and AISI 304 by underwater friction stir welding. *Journal of Manufacturing Processes*. 2019;38: 370–386.
22. Mahto RP, Anishetty S, Sarkar A, Mypati O, Pal SK, Majumdar JD. Interfacial Microstructural and Corrosion Characterizations of Friction Stir Welded AA6061-T6 and AISI304 Materials. *Metals and Materials International*. 2019;25: 752–767.
23. Chitturi V, Pedapati SR, Awang M. Effect of tilt angle and pin depth on dissimilar friction stir lap welded joints of aluminum and steel alloys. *Materials*. 2019;12(23): 3901.
24. Uematsu Y, Kakiuchi T, Ogawa D, Hashiba K. Fatigue crack propagation near the interface between Al and steel in dissimilar Al/steel friction stir welds. *International Journal of Fatigue*. 2020;138: 105706.
25. Chitturi V, Pedapati SR, Awang M. Investigation of weld zone and fracture surface of friction stir lap welded 5052 aluminum alloy and 304 stainless steel joints. *Coatings*. 2020;10(11): 1062.
26. Jabraeili R, Jafarian HR, Khajeh R, Park N, Kim Y, Heidarzadeh A, Eivani AR. Effect of FSW process parameters on microstructure and mechanical properties of the dissimilar AA2024 Al alloy and 304 stainless steel joints. *Materials Science and Engineering A*. 2021;814: 140981.
27. Wang J, Ling X, Zhang W, Lu X, Chen C. Microstructures and mechanical properties of friction stir welded butt joints of 3003-H112 aluminum alloy to 304 stainless steel used in plate-fin heat exchanger. *Journal of Materials Research and Technology*. 2022;21: 3086–3097.
28. Joshani E, Beidokhti B, Davodi A, Amelzadeh M. Evaluation of dissimilar 7075 aluminum/AISI 304 stainless steel joints using friction stir welding. *Journal of Alloys and Metallurgical Systems*. 2023;3: 100017.
29. Datta A, Shrivastava A, Mandal N, Roy H, Chakraborty SS. A comparative investigation of butt friction stir welding of aluminium alloys, AA 1100 and AA 7075, with AISI 304 stainless steel. *Welding in the World*. 2023;67: 1449–1465.
30. Kumar R, Manjaiah M, Davidson MJ. The effect of friction stir welding on the microstructure and mechanical properties of the dissimilar SS304 and Al7075-T6 alloy joints. *Welding International*. 2023;37(11): 643–654.
31. Ou W, Guo G, Cui C, Zhang Y, Qian L. Heat transfer in aluminum-steel joint and weld tool during the friction stir welding: Simulation and experimental validation. *The International Journal of Advanced Manufacturing Technology*. 2023;125: 2211–2224.
32. Mir FA, Khan NZ, Mukhtar Z, Badruddin IA, Kamangar S, Nisar L. Friction stir welding of AA2024-T3 and SS304 alloys: microstructural analysis, microhardness evaluation, and tensile performance. *Physica Scripta*. 2024;99(10): 105970.
33. Zhang M, Liu JM, Xue P, Liu FC, Wu LH, Ni DR, Xiao BL, Wang KS, Ma ZY. Eliminating Cu-rich intermetallic compound layer in dissimilar friction stir welding of 304 stainless steel and 2219 Al alloy via ultralow rotation speed. *Journal of Materials Processing Technology*. 2024;329: 118444.
34. Nakrani J, Yan W, Shrivastava A. Fatigue crack growth behavior in SS304-Al5083 dissimilar friction stir welded joints. *Procedia Structural Integrity*. 2024;61: 188–194.
35. Caetano GDQ, Andrade TC, Motta MF, Miranda HC, Farias JP, Bergmann LA, Dos Santos JF, Silva CC. Assessment of the joint configuration and welding parameters for the dissimilar joining of AISI 304L and AISI 410S stainless steels by friction stir welding. *The International Journal of Advanced Manufacturing Technology*. 2024;133: 5691–5703.
36. Kumar A, Bansal SN, Chandraker R. Computational modeling of blast furnace cooling stave based on heat transfer analysis. *Materials Physics and Mechanics*. 2012;15(1): 46–65.
37. Yadav A, Jain A, Verma R. Effect of tilt angle for conical pin tool with a conical shoulder on heat transfer and material flow using numerical simulation in friction stir welding. *Materials Physics and Mechanics*. 2023;51(3): 126–145.
38. Yadav A, Jain A, Verma R. Numerical Simulation of Friction Stir Welding Process to Investigate the Effect of a Conical Pin Tool with a Flat and Conical Shoulder on Heat Transfer. *NanoWorld Journal*. 2023;9(S1): S239–S242.
39. Hasan AF. CFD modelling of friction stir welding (FSW) process of AZ31 magnesium alloy using volume of fluid method. *Journal of Materials Research and Technology*. 2019;8(2): 1819–1827.
40. Yadav A, Jain A, Verma R. Rotational Speed Influence on Weld Temperature in Friction Stir Lap Joint of Aluminium Alloy 6061 Using Numerical Simulation. *Journal of Polymer and Composites*. 2024;12(S02): 235–245.
41. Nandan R, Roy GG, DebRoy T. Numerical simulation of three dimensional heat transfer and plastic flow during friction stir welding. *Metallurgical and Materials Transactions A*. 2006;37: 1247–1259.
42. Yang CL, Wu CS, Lv XQ. Numerical analysis of mass transfer and material mixing in friction stir welding of aluminum/magnesium alloys. *Journal of Manufacturing Processes*. 2018;32: 380–394.
43. Nandan R, Roy GG, Lienert TJ, DebRoy T. Numerical modelling of 3D plastic flow and heat transfer during friction stir welding of stainless steel. *Science and Technology of Welding and Joining*. 2006;11(5): 526–537.

44. Thomas WM, Johnson KI, Wiesner CS. Friction stir welding—recent developments in tool and process technologies. *Advanced Engineering Materials*. 2003;5(7): 485–490.
45. Sheppard T, Wright DS. Determination of flow stress: Part 1 constitutive equation for aluminium alloys at elevated temperatures. *Metallurgical Technology*. 1979;6(1): 215–223.
46. Sheppard T, Jackson A. Constitutive equations for use in prediction of flow stress during extrusion of aluminium alloys. *Materials Science and Technology*. 1997;13(3): 203–209.
47. Tello KE, Gerlich AP, Mendez PF. Constants for hot deformation constitutive models for recent experimental data. *Science and Technology of Welding and Joining*. 2010;15(3): 260–266.
48. Hasan AF, Bennett CJ, Shipway PH, Cater S, Martin J. A numerical methodology for predicting tool wear in friction stir welding. *Journal of Materials Processing Technology*. 2017;241: 129–140.
49. Darvazi AR. A semi-analytical solution for temperature distribution in friction stir welding. To be published in *The International Journal of Advanced Manufacturing Technology*. [Preprint] 2021. Available from: doi.org/10.21203/rs.3.rs-521499/v1
50. Sadeghian B, Taherizadeh A, Atapour M. Simulation of weld morphology during friction stir welding of aluminum–stainless steel joint. *Journal of Materials Processing Technology*. 2018;259: 96–108.
51. Hamilton C, Dymek S, Sommers A. A thermal model of friction stir welding in aluminum alloys. *International Journal of Machine Tools and Manufacture*. 2008;48(10): 1120–1130.
52. Neto DM, Neto P. Numerical modeling of friction stir welding process: A literature review. *The International Journal of Advanced Manufacturing Technology*. 2013;65: 115–126.
53. Zhang J, Shen Y, Li B, Xu H, Yao X, Kuang B, Gao J. Numerical simulation and experimental investigation on friction stir welding of 6061-T6 aluminum alloy. *Materials & Design*. 2014;60: 94–101.
54. Saravanakumar R, Rajasekaran T, Pandey C. Effects of welding parameter on the microstructure and mechanical properties of friction stir-welded non-heat treatable alloy AA5083. *Journal of Adhesion Science and Technology*. 2026;40(3): 631–649.
55. Kumar R, Upadhyay V, Pandey C. Effect of post-weld heat treatments on microstructure and mechanical properties of friction stir welding joints of AA2014 and AA7075. *Journal of Materials Engineering and Performance*. 2023;32: 10989–10999.
56. Saravanakumar R, Rajasekaran T, Pandey C. Optimisation of underwater friction stir welding parameters of aluminum alloy AA5083 using RSM and GRA. *Proceedings of the Institution of Mechanical Engineers, Part E: Journal of Process Mechanical Engineering*. 2023;237(6): 2334–2348.
57. Saravanakumar R, Rajasekaran T, Pandey C. Underwater friction stir welded armour grade AA5083 aluminum alloys: experimental ballistic performance and corrosion investigation. *Journal of Materials Engineering and Performance*. 2023;32: 10175–10190.